fractal and fractional

MDPI

Article

Multifractal Characterization of Heterogeneous Pore Water Redistribution and Its Influence on Permeability During Depletion: Insights from Centrifugal NMR Analysis

Fangkai Quan [1,2,*], Wei Lu [1], Yu Song [3], Wenbo Sheng [1], Zhengyuan Qin [4] and Huogen Luo [1,*]

[1] Scientific Research and Development Platform of Technology of Disaster Prevention in Deep Coal Mines, Anhui University of Science and Technology, Huainan 232000, China
[2] State Key Laboratory for Safe Mining of Deep Coal and Environmental Protection, Ltd., Huainan 232000, China
[3] Key Laboratory of Coalbed Methane Resources & Reservoir Formation Process, Ministry of Education, China University of Mining and Technology, Xuzhou 221116, China
[4] Department of Mechanical, Materials and Manufacturing Engineering, Faculty of Engineering, University of Nottingham, Nottingham NG7 2RD, UK
* Correspondence: k_quanf@foxmail.com (F.Q.); luohuogenzyq@sina.com (H.L.)

Abstract

The dynamic process of water depletion plays a critical role in both surface coalbed methane (CBM) development and underground gas extraction, reshaping water–rock interactions and inducing complex permeability responses. Addressing the limited understanding of the coupling mechanism between heterogeneous pore water evolution and permeability during dynamic processes, this study simulates reservoir transitions across four zones (prospective planning, production preparation, active production, and mining-affected zones) via centrifugal experiments. The results reveal a pronounced scale dependence in pore water distribution. During low-pressure stages (0–0.54 MPa), rapid drainage from fractures and seepage pores leads to a ~12% reduction in total water content. In contrast, high-pressure stages (0.54–3.83 MPa) promote water retention in adsorption pores, with their relative contribution rising to 95.8%, forming a dual-structure of macropore drainage and micropore retention. Multifractal analysis indicates a dual-mode evolution of movable pore space. Under low centrifugal pressure, D_{-10} and $\Delta\alpha$ decrease by approximately 34% and 36%, respectively, reflecting improved connectivity within large-pore networks. At high centrifugal pressure, an ~8% increase in $D_0 - D_2$ suggests that pore-scale heterogeneity in adsorption pores inhibits further seepage. A quantitative coupling model establishes a quadratic relationship between fractal parameters and permeability, illustrating that permeability enhancement results from the combined effects of pore volume expansion and structural homogenization. As water saturation decreases from 1.0 to 0.64, permeability increases by more than 3.5 times. These findings offer theoretical insights into optimizing seepage pathways and improving gas recovery efficiency in dynamically evolving reservoirs.

Keywords: multifractal analysis; pore water heterogeneity; pore network connectivity; coalbed methane; reservoir development

Academic Editor: Alex Elías-Zúñiga

Received: 23 April 2025
Revised: 11 July 2025
Accepted: 9 August 2025
Published: 15 August 2025

Citation: Quan, F.; Lu, W.; Song, Y.; Sheng, W.; Qin, Z.; Luo, H. Multifractal Characterization of Heterogeneous Pore Water Redistribution and Its Influence on Permeability During Depletion: Insights from Centrifugal NMR Analysis. *Fractal Fract.* **2025**, *9*, 536. https://doi.org/10.3390/fractalfract9080536

1. Introduction

The dynamic evolution of pore fluid distribution and its coupling with permeability in heterogeneous reservoirs are critical scientific challenges in optimizing hydrocarbon

recovery and enhancing energy extraction efficiency [1–3]. During reservoir development, progressive drainage of pore water—induced by changes in pressure gradients as the system transitions from prospective planning zones to mining-affected zones—fundamentally alters water–rock interactions and the connectivity of the pore network [4,5]. Although numerous investigations have detailed static reservoir characteristics—porosity, permeability, and variations in rock texture—the processes that drive pore water movement throughout different stages of reservoir evolution are still not well understood [6–8].

Conventional reservoir models often oversimplify pore water distribution by treating it as homogeneous or by assuming linear relationships between water saturation and permeability [9–11]. However, both field observations and laboratory experiments demonstrate that drainage induces highly nonuniform fluid migration across multiscale pore–fracture systems, driven by capillary forces, adsorption phenomena, and complex pore throat geometries [12,13]. For instance, in coalbed methane (CBM) reservoirs, the expulsion of free water from fractures and macropores during early production stages is followed by the retention of adsorbed water in nanopores, creating spatially heterogeneous fluid distributions [14,15]. These irregular distributions not only impair gas flow but also concentrate stresses in specific zones, heightening the potential for localized reservoir damage. Beyond affecting water retention and drainage, such multiscale heterogeneity—especially when exhibiting multifractal characteristics—can also influence other critical performance aspects in CBM development. These include gas adsorption/desorption behavior, fluid connectivity, effective permeability, and stress-sensitive compaction behavior.

Furthermore, studies in ecological and environmental systems, such as wetland soil modeling, have adopted the Richards equation to simulate moisture dynamics under variable saturation conditions [16]. However, such methods are often less effective in coal reservoir settings due to the fundamentally different pore structure and flow mechanisms. Despite these implications, existing frameworks lack quantitative tools to resolve the scale-dependent fluid redistribution patterns and their nonlinear impacts on permeability [17,18].

Recent advances in fractal theory offer promising avenues to address these limitations. Fractal geometry, particularly multifractal analysis, enables the quantification of complex pore structures and fluid distributions by capturing hierarchical heterogeneity across multiple scales [19]. When integrated with advanced imaging techniques like low-field nuclear magnetic resonance (LF-NMR), fractal parameters can delineate dynamic fluid migration pathways and predict permeability responses under varying drainage conditions [20,21]. Nevertheless, current applications of fractal theory in reservoir studies predominantly focus on static pore structure characterization, with limited exploration of its utility in modeling transient fluid behavior during reservoir transition phases [22–24]. Furthermore, the coupling mechanisms between fractal-derived pore network attributes (e.g., connectivity, heterogeneity) and macroscopic permeability remain underexplored, particularly in the context of multizone reservoir development [25].

To bridge these gaps, this study investigates the multifractal evolution of pore water distribution and its control on permeability during reservoir transition across four critical zones: prospective planning, production preparation, production, and mining-affected zones. Centrifugal experiments were designed to simulate reservoir drainage processes under incremental pressures (0.54–3.83 MPa), replicating the dynamic pressure gradients encountered during field-scale exploitation [26]. LF-NMR was employed to track spatial-temporal variations in pore water saturation, while multifractal theory was applied to quantify the heterogeneity and connectivity of movable pore spaces. Key objectives included the following: (1) elucidating scale-dependent pore water redistribution mechanisms during reservoir transition; (2) establishing multifractal parameter permeability

relationships to decode the structural controls on fluid flow; and (3) developing predictive models for permeability evolution under variable water saturation conditions.

This work deepens our theoretical insight into how fluid movement and pore structure interact over time in variable reservoirs and introduces a fractal-based framework for refining drainage strategies. The main contributions of this work are as follows: (1) simulating multistage CBM drainage processes using centrifugal NMR to represent various production stages; (2) quantifying pore water heterogeneity and its evolution through multifractal analysis; and (3) establishing a multifractal–permeability coupling model to reveal the controlling role of pore structure on flow behavior. By connecting small-scale variations in pore water distribution to large-scale permeability changes, our findings deliver practical tools to reduce permeability hysteresis and boost recovery efficiency across multizone reservoir systems.

2. Materials and Methods

2.1. Sample Collection and Preparation

Coal samples were collected from a fresh mining face of the No. 8 coal seam in an active mining area. To preserve sample integrity and minimize artificial fracturing during transportation, the collected coal blocks were triple-wrapped using cling film, opaque black plastic film, and foam padding. The samples were promptly transported to a laboratory for coring. Cores were drilled parallel to the coal bedding plane using a 2.5 cm inner diameter drill bit and cut into cylindrical specimens of 5 cm length. Both ends of the cores were polished to ensure flat surfaces for subsequent testing. Residual samples were sent to the Jiangsu Institute of Geological and Mineral Exploration and Design for basic physicochemical characterization, including proximate analysis and vitrinite reflectance measurements. Key parameters are summarized in Table 1.

Table 1. Basic physical parameters of samples.

Sample ID	$R_{o,max}$ (%)	A_d (%)	V_{daf} (%)	FC_d (%)	Vitrinite (%)	Inertinite (%)	Exinite (%)
8-2	0.72	4.32	32.25	58.33	58.3	41.2	0.5

Notes: $R_{o,max}$ is mean maximum vitrinite reflectance; A_d is ash yield (dry basis); V_{daf} is volatile matter (dry ash-free basis); FC_d is fixed carbon (dry basis); vitrinite, inertinite, and exinite contents are expressed as percentages of total maceral composition.

2.2. Experimental Methods

2.2.1. Centrifugal Drainage Simulation

A high-speed centrifuge was employed to simulate reservoir drainage processes under incremental pressure conditions [27]. The centrifugal pressure difference between two immiscible fluids at varying rotational speeds corresponds to capillary pressure. Following the industry standard rock capillary pressure measurement (SY/T 5346-2005) [28], capillary pressure (p_{ci}) was calculated as:

$$p_{ci} = 1.097 \times 10^{-9} \Delta\rho L(Re - \frac{L}{2})n^2 \quad (1)$$

where p_{ci} is the capillary pressure (MPa); $\Delta\rho$ is the fluid density difference (g/cm^3), which is 1 g/cm^3 in the centrifugal experiments conducted in this study; L is the sample length (cm), set as 5 cm for the sample used in this study; R_e is the centrifuge rotor radius (cm), which is 13.5 cm for the high-performance core centrifuge employed; and n is the rotational speed (rpm). Based on equipment specifications, rotational speeds of 3000, 4000, 5000, 6000, 7000, and 8000 rpm were applied to generate equivalent drainage pressures of 0.54,

0.96,1.49, 2.15, 2.93, and 3.83 MPa. Low-pressure stages simulate early-stage drainage behavior in the planning and preparation zones, highlighting the rapid expulsion of water from macropores. In contrast, high-pressure conditions simulate active and mining-affected zones, confirming the persistence of micropore-bound water.

The primary LF–NMR acquisition parameters were as follows: echo spacing = 0.2 ms; number of echoes = 2048; wait time = 3 s; temperature = 23 °C; number of iterations = 5000; and number of scans = 64. Prior to testing, the NMR device was calibrated using a standard sample of known water mass (0.05, 0.30, 0.60, 1.50, 2.00, and 2.50 g) to establish a linear relationship between magnetization amplitude and fluid volume ($R^2 > 0.99$), as shown in previous study [29]. Post-centrifugation, each sample underwent LF-NMR T_2 spectrum analysis and gas permeability measurement.

2.2.2. Gas Permeability Measurement

Gas-phase permeability was measured under a confining pressure of 10 MPa using the steady-state method outlined in core analysis methods (SY/T 5336-2006) [30]. A pressure regulator maintained constant inlet pressure, while a flowmeter monitored gas flux until stabilization. The pressure differential (Δp) and flow rate (q) across the core were recorded, and permeability (k) was calculated via the compressible-fluid (gas) Darcy equation [30]:

$$k = \frac{2p_a \mu q L}{A(p_i^2 - p_o^2)} \times 100 \quad (2)$$

where k is permeability (mD); p_a is atmospheric pressure (MPa); p_i and p_o are inlet and outlet pressures (MPa); L is core length (cm); μ is nitrogen viscosity (cP); q is gas flow rate at atmospheric pressure (cm^3/s), and A is cross-sectional area (cm^2).

2.3. Data Processing Methods

2.3.1. Single Fractal Analysis Based on LF-NMR

Fractal geometry, since its inception, has been widely adopted as a mathematical tool to characterize complex systems with scale-invariant properties [31]. Coal pores exhibit intrinsic fractal characteristics, which can be quantified using low-field nuclear magnetic resonance (LF-NMR) by analyzing the transverse relaxation time (T_2) distribution of pore fluids. For water-saturated coal reservoirs, the relationship between T_2 and pore radius (r) is governed by:

$$T_2 = \rho \cdot \frac{r}{S/V} \quad (3)$$

where ρ is the surface relaxivity (μm/ms); and S/V represents the pore surface-to-volume ratio (μm^{-1}). For spherical pores, $S/V = 3/r$, leading to:

$$T_2 = \frac{\rho}{3} \cdot r \Rightarrow r = C \cdot T_2 \ (C = 3/\rho) \quad (4)$$

Thus, pore radius scales linearly with T_2. The fractal nature of coal pores implies that their volumetric distribution follows a power law scaling relationship:

$$N(>r) \propto r^{-D} \quad (5)$$

where D is the fractal dimension ($2 < D$) and $N(>r)$ denotes the number of pores with radii exceeding r. Differentiating $N(>r)$ yields the pore volume distribution function:

$$dV(r) \propto r^{2-D} dr \quad (6)$$

Substituting $r = C \cdot T_2$, the volume distribution in terms of becomes:

$$dV(T_2) \propto \left(C \cdot T_2\right)^{2-D} \cdot C \cdot dT_2 = C^{3-D} \cdot T_2^{2-D} dT_2 \tag{7}$$

Integrating T_2 from 0 to, $T_{2,\max}$, the total pore volume is expressed as:

$$V_{\text{total}} \propto C^{3-D} \int_0^{T_{2,max}} T_2^{2-D} dT_2 \tag{8}$$

The cumulative volume fraction $V(T_2)$, representing the proportion of pores with T_2 values below a threshold, is derived as:

$$V(T_2) = \frac{\int_0^{T_2} T'^{2-D} dT'}{\int_0^{T_{2,max}} T'^{2-D} dT'} = \left(\frac{T_2}{T_{2,max}}\right)^{3-D} \tag{9}$$

Taking the logarithm of both sides yields:

$$\lg V(T_2) = (3-D) \cdot \lg T_2 - (3-D) \cdot \lg T_{2,max} \tag{10}$$

A linear fit to the $\lg V(T_2)$ vs. $\log T_2$ plot provides the fractal dimension D, where the slope equals $3-D$.

2.3.2. Multifractal Analysis

Unlike single fractal models, multifractal theory resolves hierarchical heterogeneity by decomposing complex systems into subsets with distinct scaling behaviors [32]. This approach characterizes pore structures through the multifractal singularity spectrum (α~$f(\alpha)$) and generalized dimension spectrum (q~$D(q)$), calculated as follows.

The total pore size range L is divided into subintervals L_{i} of equal length ε. The probability density $P_{\text{i}}(\varepsilon)$ for each subinterval is defined as:

$$P_i(\varepsilon) = \frac{N_i(\varepsilon)}{N_t} = \frac{Ni(\varepsilon)}{\sum_{i=1}^{N(\varepsilon)} Ni(\varepsilon)} \propto \varepsilon^{\alpha i} \tag{11}$$

where N_{i} is the pore volume within L_{i}, and N_{t} is the total pore volume.

The number of subintervals N_α (ε) sharing a common singularity strength α scales as [33]:

$$N_\alpha(\varepsilon) \propto \varepsilon^{-f(\alpha)} \tag{12}$$

where $f(\alpha)$, the multifractal spectrum, is a convex function for multifractal systems but constant for monofractals [34]. The singularity strength $\alpha(q)$ and spectrum $f(\alpha)$ are computed via:

$$\alpha(q) \propto \frac{\sum_{i=1}^{N(\varepsilon)} \mu_i(q,\varepsilon) \lg[P_i(\varepsilon)]}{\lg(\varepsilon)} \tag{13}$$

$$f[\alpha(q)] \propto \frac{\sum_{i=1}^{N(\varepsilon)} \mu_i(q,\varepsilon) \lg[\mu_i(q,\varepsilon)]}{\lg(\varepsilon)} \tag{14}$$

where $\mu_i(q,\varepsilon)$, the probability measure weighted by moment order q, is:

$$\mu_i(q,\varepsilon) = \frac{P_i^q(\varepsilon)}{\sum_{i=1}^{N(\varepsilon)} P_i^q(\varepsilon)} \tag{15}$$

By varying q within [−10,10], $\alpha(q)$ and $f(\alpha)$ are parameterized.

The partition function $\chi(q,\varepsilon)$ and generalized dimension D_q are defined as:

$$\chi(q,\varepsilon) = \sum_{i}^{Ni} P_i^q(\varepsilon) \propto \varepsilon^{-(q-1)Dq} \tag{16}$$

$$Dq = \frac{1}{q-1}\lim_{\varepsilon\to 0}\frac{\lg\sum_{i=1}^{N(\varepsilon)} P_i^q(\varepsilon)}{\lg\varepsilon} = \frac{\tau(q)}{q-1} \tag{17}$$

$$\tau(q) = (q-1)Dq = \lim_{\varepsilon\to 0}\frac{\lg\sum_{i=1}^{N(\varepsilon)} P_i^q(\varepsilon)}{\lg\varepsilon} \tag{18}$$

For $q < 0$, Dq emphasizes regions with high pore volume probability density (e.g., adsorption pores), while $q > 0$ highlights low-density regions (e.g., fractures). Specific dimensions include the following: capacity dimension (D_0) reflects global pore heterogeneity; information dimension (D_1) measures entropy-related structural complexity; correlation dimension (D_2) quantifies pore connectivity.

The singularity strength range $\Delta\alpha$, a key metric for pore heterogeneity, is calculated as [35]:

$$\Delta\alpha = \alpha_{\max} - \alpha_{\min} \tag{19}$$

Larger $\Delta\alpha$ values indicate stronger multifractality and structural diversity.

Multifractal calculations were performed using MATLAB R2022a (MathWorks) with custom scripts based on Equations (11)–(19). Statistical analysis and figure generation utilized OriginPro 2023 (OriginLab).

Data fitting of analytical relationships was performed using Origin 2022 software with a least-squares regression algorithm. Both linear and nonlinear (power law) fitting models were applied based on trend characteristics, with R^2 values used to assess fit quality.

3. Results and Discussion

3.1. Spatial Distribution Characteristics of Pore Water During Reservoir Drainage

The T_2 relaxation spectra and associated pore water distribution patterns under incremental centrifugal forces (0–3.83 MPa) reveal a dynamic two-stage depletion mechanism (Figure 1, Table 2). The total spectral area, representing pore water volume, decreased by 36.1% (193,978.36 a.u to 123,937.35 a.u.), with distinct behavioral regimes governed by pore-scale capillary and adsorption dynamics.

Based on the response characteristics of hydrogen signal relaxation times in the NMR T_2 spectrum to different pore-fracture sizes, the pore-fracture system in coal can be classified into three categories: pores with $T_2 < 2.5$ ms correspond to micropores with sizes ranging from 0 to 10^2 nm, which are defined as adsorption pores; pores with 2.5 ms < T_2 < 100 ms correspond to mesopores and macropores with sizes between 10^2 and 10^4 nm, identified as seepage pores; and $T_2 > 100$ ms corresponds to fractures larger than 10^4 nm. Among them, adsorption pores primarily provide adsorption space for methane molecules and influence the gas-bearing capacity of the coal reservoir, while seepage pores and fractures together constitute the main migration pathways for reservoir fluids [36–38]

In the low-pressure regime (0–0.54 MPa), a rapid 11.8% reduction in total water content occurred, predominantly driven by the expulsion of free water from macropores (seepage pores and fractures). These large-aperture features exhibited low capillary entry pressures, enabling efficient fluid mobilization under minimal centrifugal forces. Fracture systems demonstrated particular susceptibility to drainage, losing 90.7% of their initial water volume (2164.60 to 200.53 a.u.) within this stage. This abrupt drainage aligns with

field observations of early water production during coalbed methane extraction, where fractures serve as primary conduits for initial fluid flow.

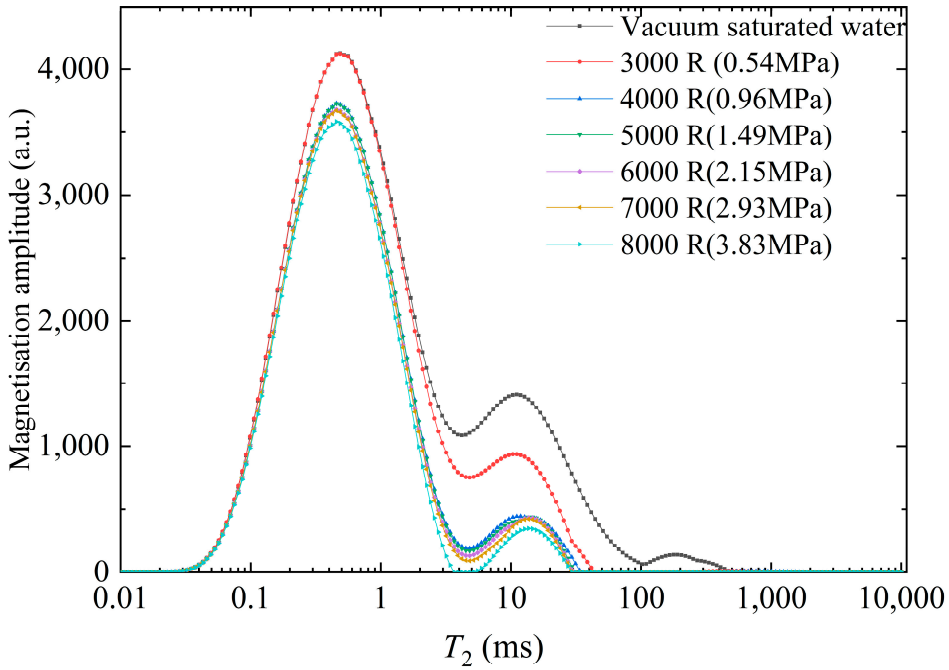

Figure 1. T_2 Relaxation spectra of pore water distribution under different drainage conditions.

Table 2. Dynamic changes of pore water in reservoir samples under different displacement pressures.

Displacement Pressure (MPa)	Total T_2 Area (a.u.)	Adsorption Pores (a.u.)	Seepage Pores (a.u.)	Fractures (a.u.)
0.00	193,978.36	152,267.14	39,546.62	2164.60
0.54	171,162.30	149,172.98	21,788.78	200.53
0.96	136,595.25	127,252.43	9198.12	144.70
1.49	135,396.04	126,945.55	8447.69	2.80
2.15	132,623.29	124,795.68	7825.95	1.66
2.93	130,951.44	123,897.22	7052.60	1.62
3.83	123,937.35	118,806.42	5130.77	0.16

Transitioning to the high-pressure regime (0.96–3.83 MPa), water depletion kinetics decelerated markedly. Residual water became increasingly localized in adsorption pores and micropores (radii < 100 nm), where surface interactions and capillary confinement mechanisms dominate. Notably, adsorption pores exhibited counterintuitive behavior. Although their absolute water content decreased by 22.0% (152,267.14 to 118,806.42 a.u.), their relative contribution surged from 78.5% to 95.8% of total water storage (Figure 2). This inversion highlights the critical role of strong physisorption at oxygen-functionalized coal surfaces (e.g., hydroxyl, carboxyl groups), where water molecules form hydrogen-bonded networks requiring energy inputs exceeding typical mechanical displacement thresholds. The near-constant depletion behavior observed in the high-pressure range (0.96–3.83 MPa) can be attributed to the dominance of adsorbed water in micropores. These water molecules exhibit strong hydrogen bonding and capillary confinement, resisting mobilization even under elevated centrifugal pressure. This contrasts with the rapid drainage of free water in macropores at lower pressures. It is hypothesized that further increasing pressure beyond 3.83 MPa may induce a secondary desorption phase, though this remains to be confirmed in future research.

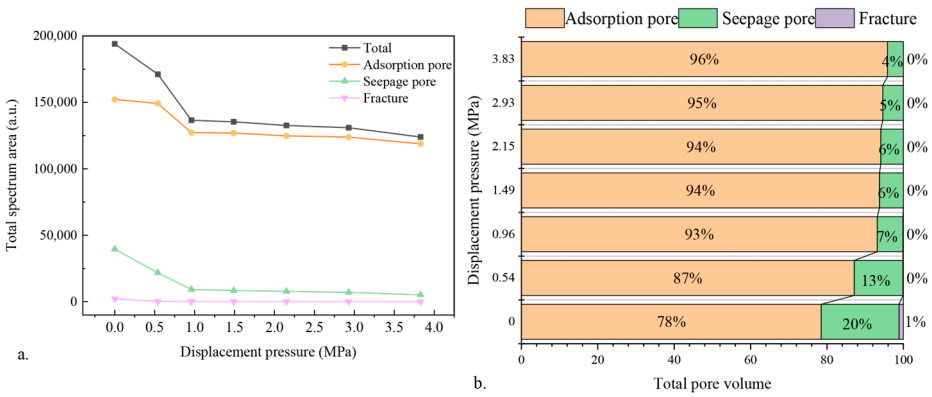

Figure 2. (**a**,**b**) Dynamic characteristics of pore water distribution during centrifugal drainage.

The volume of seepage pores plummets from 39,546.62 to 5130.77 a.u., representing an 87.0% reduction. Once the pressure exceeds 0.54 MPa, their contribution to the total water content drops below 5%. As the primary transport channels within the pore network, the rapid depletion of water from these seepage pores directly diminishes the effective water-phase permeability of the reservoir. This indicates that, when the displacement pressure surpasses 0.54 MPa, spontaneous water flow within the coal reservoir may cease, transitioning effectively to a bound water state.

The water signal in fracture spaces almost completely vanishes—from 2164.60 to just 0.16 a.u. (a 99.9% reduction). At 1.49 MPa, the fractures are nearly emptied (only 2.80 a.u. remaining). This rapid depletion (a 90.7% reduction within 0–0.54 MPa) confirms the critical role of fractures in initial seepage capacity. However, their extremely low residual water content (<0.1%) indicates that water in fractures is readily expelled during production, allowing gas-phase permeability to dominate.

Figure 3a shows that, under saturation (0 MPa displacement pressure), pore water is continuously and evenly distributed across the sample cross-section, with high-intensity NMR signals (indicated by bright regions). Combined with T_2 spectral data (Table 2), it is evident that areas with developed fractures exhibit much stronger signals than the coal matrix, confirming the water-enriching role of fracture systems. These correspond to T_2 values in the range of 10–100 ms, indicative of macroscopic fractures with openings > 1 μm. The light-yellow-green region regions dispersed throughout the matrix represent seepage pores (accounting for 20.4%) forming secondary seepage networks, with T_2 values mainly between 1 and 10 ms (pore diameters 50–500 nm). The adsorption pores appear as dim background regions and contribute 78.5% of the total signal. They correspond to T_2 values below 1 ms (pore diameters under 50 nm), where water molecules adhere tightly to pore surfaces. Their distribution remains relatively uniform, largely independent of variations in the surrounding coal organic matrix.

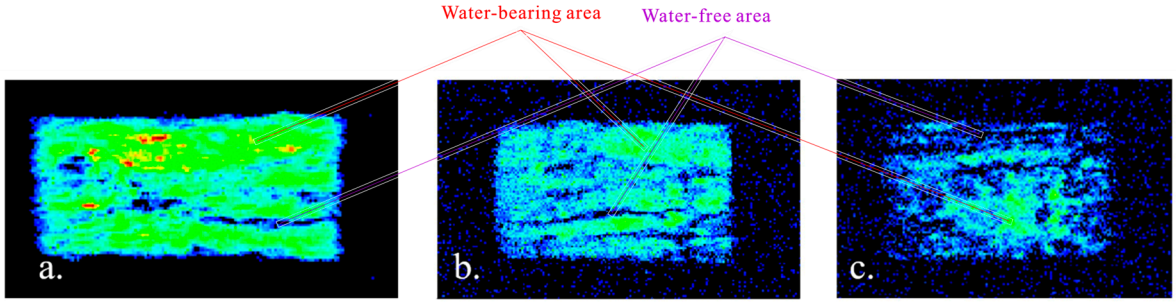

Figure 3. Dynamic variation of reservoir water distribution during centrifugation. (**a**) Saturated state; (**b**) post-3000 rpm; (**c**) post-8000 rpm.

Figure 3c shows the water distribution after applying a displacement pressure of 3.83 MPa (8000 rpm centrifugal force), where the pore water distribution undergoes significant reconstruction. The fracture systems are rapidly emptied, with signal intensity in the original fracture zones declining by more than 99%, leaving only scattered bright spots. This indicates that macroscopic fractures are fully drained under centrifugal force, and any remaining water may reside in surface asperities or be trapped within organic matter inclusions—consistent with the observed volume drop from 2164.60 to 0.16 a.u. shown in Table 2. Meanwhile, adsorption pores exhibit a selective retention of water. Although their total volume decreases by 22.0%, their spatial distribution remains relatively uniform, with some localized bright spots. This phenomenon may result from two mechanisms. First, surface adsorption effects, where oxygen-containing functional groups in the coal matrix, through hydrogen bonding, form nanoscopic water films that resist centrifugal displacement. This mechanism is supported by the established positive correlation between coal rank ($R_{o,max}$) and irreducible water saturation, as higher rank coals typically possess a greater abundance of micropores and potentially enhanced surface chemistry favoring water adsorption [39,40]. Second, pore throat bottleneck effects, where some adsorption pores with ultra-small throats (<10 nm) may experience compression or blockage during centrifugation (simulating increased effective stress), leading to localized water trapping. This aligns with observations that deeper buried coals (experiencing higher pressure) exhibit denser matrices and higher irreducible water saturation, likely due to pore compression and throat restriction [39,41]. The localized bright spots may represent regions with exceptionally high concentrations of these micropores or localized mineral/organic matter compositions favoring stronger capillary or adsorption forces.

3.2. Fractal Mechanisms Governing Pore Fluid Redistribution

To elucidate the spatial redistribution behavior of pore fluid under increasing centrifugal force, a single-fractal model was initially applied to analyze the full-scale pore system. To improve visualization, linear fits were plotted using dashed lines, and marker styles were adjusted to better distinguish data points. The slopes, fractal dimensions, and R^2 values for adsorption, seepage, and fracture pore segments are summarized in Table 3. These segment-specific regressions demonstrate the varying fractal behavior of residual water retention under different centrifugal regimes. However, as indicated by the R^2 values for "all pores" (ranging between 0.539 and 0.627), the global linear fitting was inadequate, especially in capturing the distinct regions observed in the log–log plots (Figure 4). This confirms that a single fractal dimension cannot fully represent the complex fluid distribution characteristics across varying pore structures.

To overcome this limitation and achieve a more accurate representation of the underlying fractal nature, segmented linear regression was performed separately for adsorption pores, seepage pores, and fractures (Figure 4). The corresponding slopes, fractal dimensions, and R^2 values are presented in Table 3.

To further support the use of a multifractal description, we quantitatively evaluated the variation of fitted parameters across pore types (Figure 4). For adsorption pores, the slope values (2.95–2.99) and fractal dimension D_0 (0.010–0.047) varied by less than 5%, with R^2 values consistently above 0.765. These figures reflect a relatively uniform micropore system across all tested centrifugal stages. By contrast, seepage pores showed a 3.8% increase in D from 2.882 to 2.992, with high R^2 values (mostly > 0.96), indicating growing heterogeneity while maintaining model reliability. For fractures, the fractal dimensions remained high and showed minimal variation, ranging from 2.953 to 2.968—an overall change of only ~0.5%. Corresponding R^2 values improved steadily, reaching up to 0.975 at 8000 rpm (Figure 4d). It reflects that, while free water in the fracture system is effectively

removed during centrifugal loading, the residual water distribution remains geometrically constrained, following the structural contours of the fracture network.

Table 3. Fitting results of the fractal dimension of residual water distribution in seepage pores and fractures under different centrifugal speeds.

Centrifugal Speed (rpm)		Initial State	3000R	4000R	5000R	6000R	7000R	8000R
Centrifugal Force (MPa)		0.000	0.540	0.960	1.490	2.150	2.930	3.830
All pores	Slope	1.063	1.600	1.644	1.689	1.684	1.684	1.703
	Fractal Dimension (D)	1.937	1.400	1.356	1.311	1.316	1.316	1.297
	R^2	0.539	0.621	0.621	0.627	0.626	0.626	0.627
Adsorption pores	Slope	2.990	2.968	2.958	2.959	2.954	2.955	2.953
	Fractal Dimension (D)	0.010	0.032	0.042	0.041	0.046	0.045	0.047
	R^2	0.774	0.768	0.767	0.767	0.766	0.766	0.765
Seepage pores	Slope	0.118	0.079	0.031	0.028	0.025	0.020	0.008
	Fractal Dimension (D)	2.882	2.921	2.969	2.972	2.975	2.980	2.992
	R^2	0.999	0.998	0.986	0.984	0.978	0.966	0.785
Fractures	Slope	0.047	0.048	0.035	0.038	0.037	0.036	0.032
	Fractal Dimension (D)	2.953	2.952	2.965	2.963	2.963	2.964	2.968
	R^2	0.807	0.927	0.962	0.973	0.969	0.965	0.975

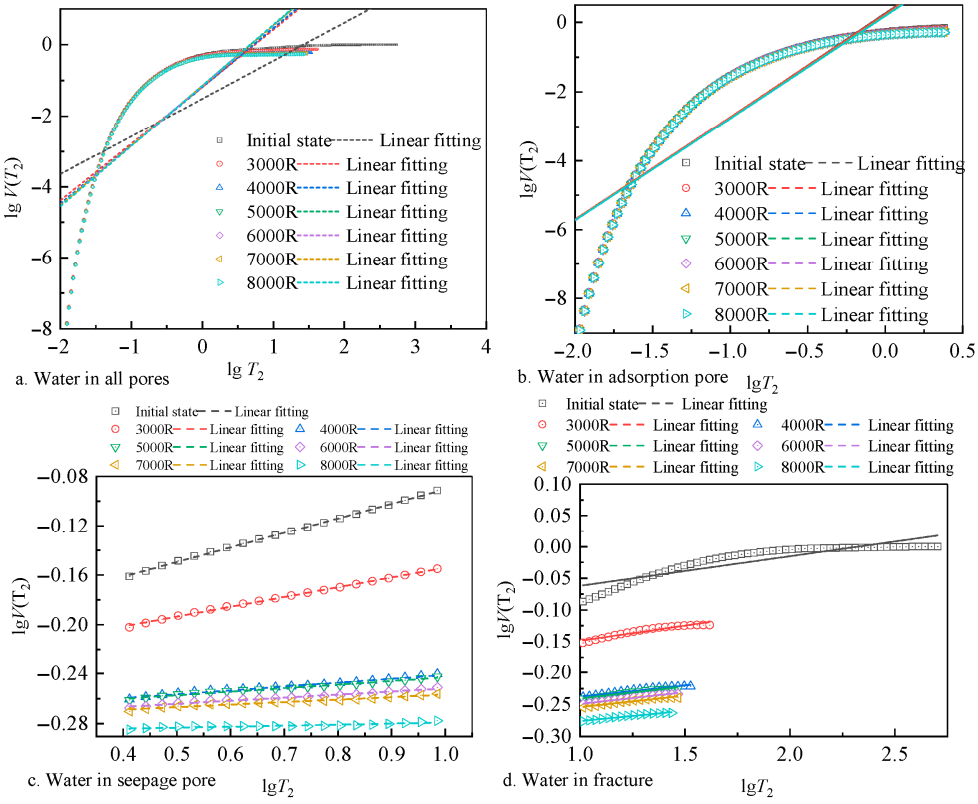

Figure 4. Fractal characteristics of residual water distribution with different centrifugal speeds (dashed lines represent the linear fitting of fractal behavior for different pore types; refer to Table 3 for fitting parameters).

These findings support a multiscale fractal framework for pore systems, where segmented fitting better captures distinct structural regimes (adsorption, seepage, and fracture). The transition from low-dimensional loosely connected regions to high-dimensional densely packed regions under centrifugal pressure underpins the evolution of pore water retention capacity and connectivity.

By subtracting the T_2 spectra of pore water under different centrifugal speeds from that under the initial saturated state, the spatial distribution spectra of the gaseous phase in the pores were obtained (see Figure 5). Figure 6 illustrates the distribution trends of gas-accessible pore space in coal reservoirs under centrifugal pressures ranging from 0.54 to 3.83 MPa. Experimental data show a nonlinear increase in total gas-accessible pore space with increasing centrifugal pressure, from 56,257 a.u. at 0.54 MPa to 103,482 a.u. at 3.83 MPa, representing an 84% increase. The growth was most pronounced between 0.54 and 1.49 MPa (+63.6%), and it gradually slowed between 1.49 and 3.83 MPa (+12.4%), suggesting that the increase in movable pore space slows as centrifugal pressure increases, indicating that the pore system is nearing its maximum capacity for fluid expulsion.

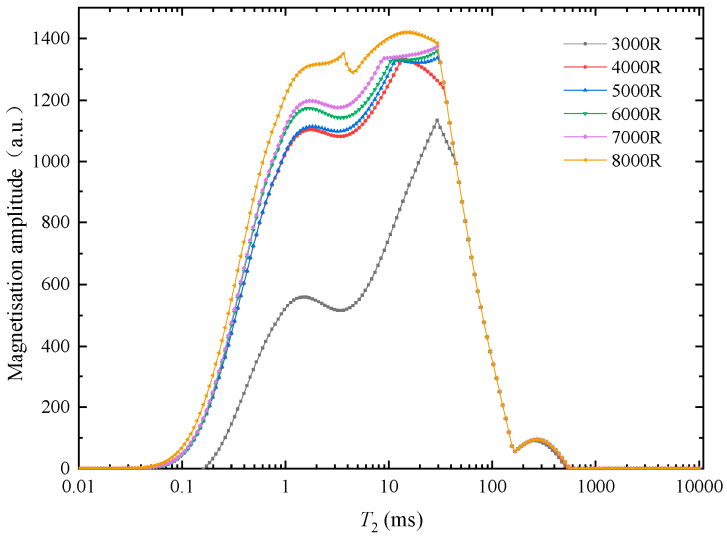

Figure 5. Distribution characteristics of gas-accessible pore space under different centrifugal speeds.

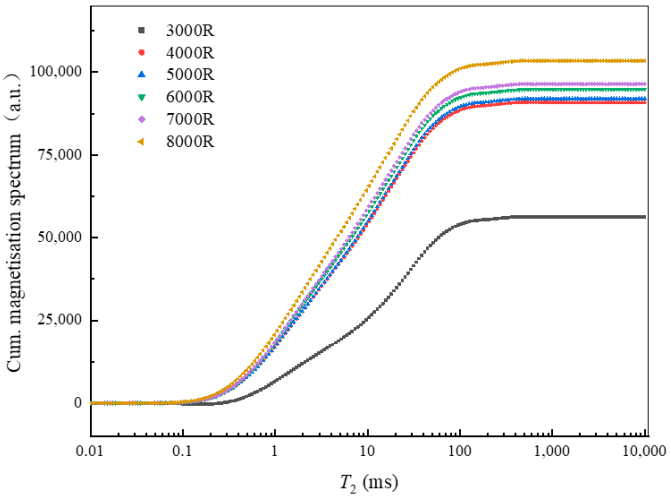

Figure 6. Cumulative distribution characteristics of gas-accessible pore space under different centrifugal speeds.

Specifically, gas-accessible space in adsorption pores increased from 13,550 to 37,469 a.u. (+176%), showing a sustained and significant enhancement, indicating that centrifugal pressure facilitates the release of adsorbed gas in micro- and nanopores. Gas-accessible space in seepage pores increased from 40,239 to 63,345 a.u. (+57.5%), with a more gradual trend, especially beyond 2.15 MPa where the growth rate diminished. Fractures only slightly increased from 2468 to 2668 a.u. (+8.1%), suggesting that fracture-related

water was largely expelled at the early stage of centrifugation, reaching the upper limit of its contribution to gas-accessible space.

The multifractal behavior of gas-accessible space under different centrifugal speeds was further analyzed to better characterize the complexity of spatial distribution. As shown in Figure 7, the multifractal spectrum reveals how the heterogeneity of the pore network evolves with increasing centrifugal pressure. Corresponding parameters extracted from the spectra are summarized in Table 4.

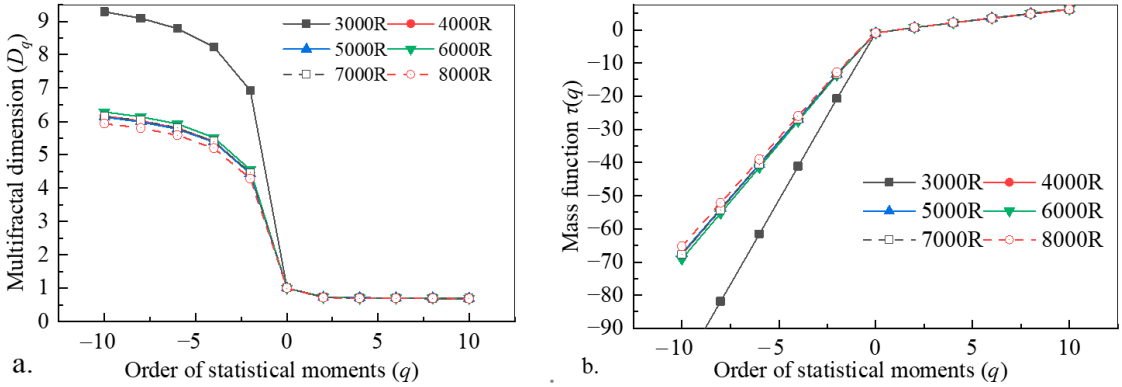

Figure 7. Multifractal characteristics of coal reservoir after different centrifugal treatments. (**a**) Multifractal dimension vs. q; (**b**) mass exponent vs. q.

Table 4. Multifractal parameters of gas-accessible space in coal samples.

Centrifugal Speed (rpm)	3000	4000	5000	6000	7000	8000
Centrifugal pressure (MPa)	0.540	0.960	1.490	2.150	2.930	3.830
D_{-10}	9.289	6.156	6.126	6.284	6.160	5.929
D_{10}	0.682	0.700	0.701	0.699	0.699	0.690
$\Delta\alpha$	9.523	6.093	6.058	6.230	6.093	5.848
D_0	1.000	1.000	1.000	1.000	1.000	1.000
D_2	0.742	0.729	0.729	0.726	0.725	0.722
D_0–D_2	0.258	0.271	0.271	0.274	0.275	0.278
D_{-10}–D_0	8.289	5.156	5.126	5.284	5.160	4.929
D_0–D_{10}	0.318	0.300	0.299	0.301	0.301	0.310
D_{-10}–D_{10}	8.606	5.456	5.425	5.584	5.461	5.239

Based on the multifractal analysis shown in Figure 7 and the corresponding parameters listed in Table 4, the evolution mechanism of gas-accessible space during reservoir development can be characterized as follows: In the low centrifugal pressure stage (0.54–1.49 MPa), the sharp decrease in D_{-10} and $\Delta\alpha$ (e.g., $\Delta\alpha$ from 9.523 to 6.058) indicates that macropores (seepage pores and fractures) are preferentially drained, resulting in more homogeneous spatial distributions. In the stability of adsorption pores, D_{10} remains stable (0.68–0.70), indicating that the structure of fine adsorption pores is not significantly disturbed, maintaining a consistent high-probability distribution pattern. In the high centrifugal pressure stage (>1.49 MPa), the fractal characteristics of adsorption pores become more prominent. The continuous increase in D_0–D_2 (from 0.271 to 0.278) suggests an enhancement in the microscopic heterogeneity within adsorption pores, possibly due to differences in pore wall roughness. The multifractal nature of pores does not only determine water migration patterns but may also regulate gas transport behavior, multiphase displacement, and the mechanical evolution of reservoir structures under stress.

In summary, the multifractal evolution of movable pore space under increasing centrifugal pressure exhibits a dual trend: macropore homogenization dominates at low centrifugal pressure with notable reductions in $\Delta\alpha$ and D_{-10}, while micropore heteroge-

nization (increase in D_0–D_2) becomes the controlling factor at higher centrifugal pressure, limiting further expansion of movable space.

Here, "homogenization" refers specifically to the observed reduction in the spatial variability and complexity of the pore network structure, as quantified by the significant decrease in the multifractal singularity spectrum width ($\Delta\alpha$, e.g., from 9.523 to 6.058, Table 4) and the capacity dimension for large pores (D_{-10}, e.g., from 9.289 to 6.126). This indicates a more uniform distribution of larger (seepage and fracture) pores and their connectivity after water drainage under low centrifugal pressure. The term "adsorption pore heterogeneity" in this context describes the increasing diversity in the gas-accessible pore size distribution within the microporous system during high-pressure drainage.

Although developed for coal, the proposed methodology has potential applications in other tight reservoirs such as shale gas and tight sandstones, where pore-scale heterogeneity and fluid redistribution under changing stress conditions are equally critical. Its application to sandstone has been validated in our prior studies [42,43], and this work extends the methodology to dynamically evolving coal systems.

3.3. Influence of Reservoir Pore Fluid Distribution on Permeability

Based on the methodology described in Section 2.1, the gas-phase permeability of the samples under different centrifugal pressure was obtained. The initial saturated state was defined as 100% water saturation, and the cumulative spectral shift after centrifugation at various speeds was used to calculate the water saturation. Accordingly, the static permeability of the reservoir at different water saturations was determined, as shown in Table 5.

Table 5. Permeability measurements of the reservoir under different centrifugal pressure.

Centrifugal Speed (rpm)	0	3000	4000	5000	6000	7000	8000	Fully Dry
Centrifugal pressure (MPa)	0	0.540	0.960	1.490	2.150	2.930	3.830	
Water saturation	1.000	0.882	0.704	0.698	0.684	0.675	0.639	0.882
Gas permeability (mD)	0.321	0.558	1.124	1.317	1.326	1.437	1.473	7.252

As shown in Figure 8, gas-phase permeability (K) increases dramatically as water saturation (S_w) decreases. Starting from a fully saturated condition (S_w = 1.0), permeability is highly suppressed due to water occupying effective flow pathways. However, once Sw falls below 0.70, permeability increases rapidly, reaching 7.25 mD under dry conditions (S_w = 0), corresponding to more than a 21-fold improvement in flow capacity. When water saturation declines to approximately 0.7, most of the free water occupying macropores is displaced, allowing for the formation of continuous gas pathways. This results in a rapid increase in effective permeability. The observed threshold behavior is consistent with the seepage theory in porous media, where a critical desaturation triggers a structural transition in flow connectivity. Exponential fitting with dry state reference yields an excellent match ($R^2 > 0.99$), validating the role of this saturation value as a physical turning point.

To characterize this nonlinear behavior, we adopted an empirical exponential model:

$$K = 7.839e^{-2.707sw} \left(R^2 \geq 0.99\right) \quad (20)$$

The rationale for selecting an exponential form lies in both empirical consistency and physical interpretation. Numerous studies have established that permeability is often exponentially related to porosity in heterogeneous porous media [44,45]. In partially saturated conditions, water saturation effectively reflects the fraction of pore space occupied by the wetting phase, and thus inversely indicates the effective porosity available for gas

flow. From this perspective, S_w functions as a proxy for the gas-phase-accessible pore volume, making the exponential model a physically meaningful choice.

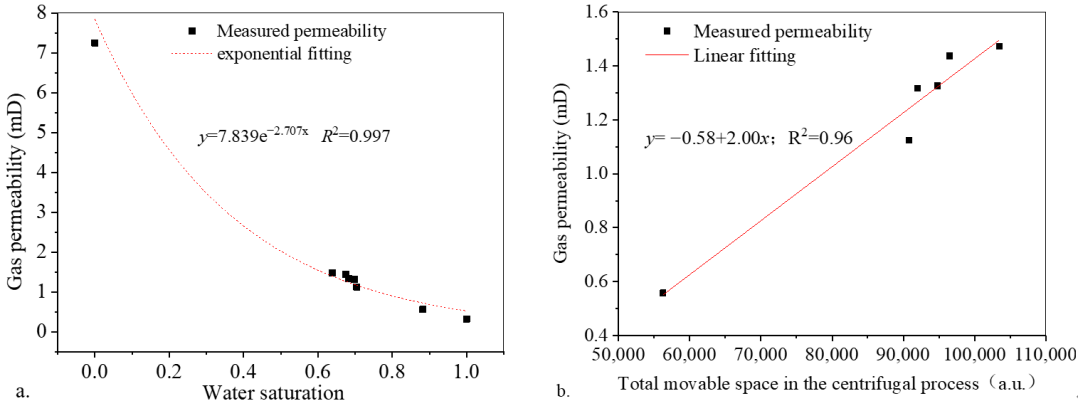

Figure 8. Relationship between gas permeability with (**a**) water saturation and (**b**) mobile pore space.

The fitting analysis of the experimental data reveals a significant coupling between gas-phase permeability and multifractal parameters characterizing the coal reservoir pore structure, uncovering the complex control mechanisms of pore heterogeneity, connectivity, and fluid distribution on gas transport. Specifically, permeability is inversely proportional to D_{-10} and $\Delta\alpha$, directly proportional to D_{10}, and highly positively correlated with D_0-D_2. These findings can be systematically interpreted from the perspectives of fractal geometry and the dynamic evolution of the pore network (Figure 9).

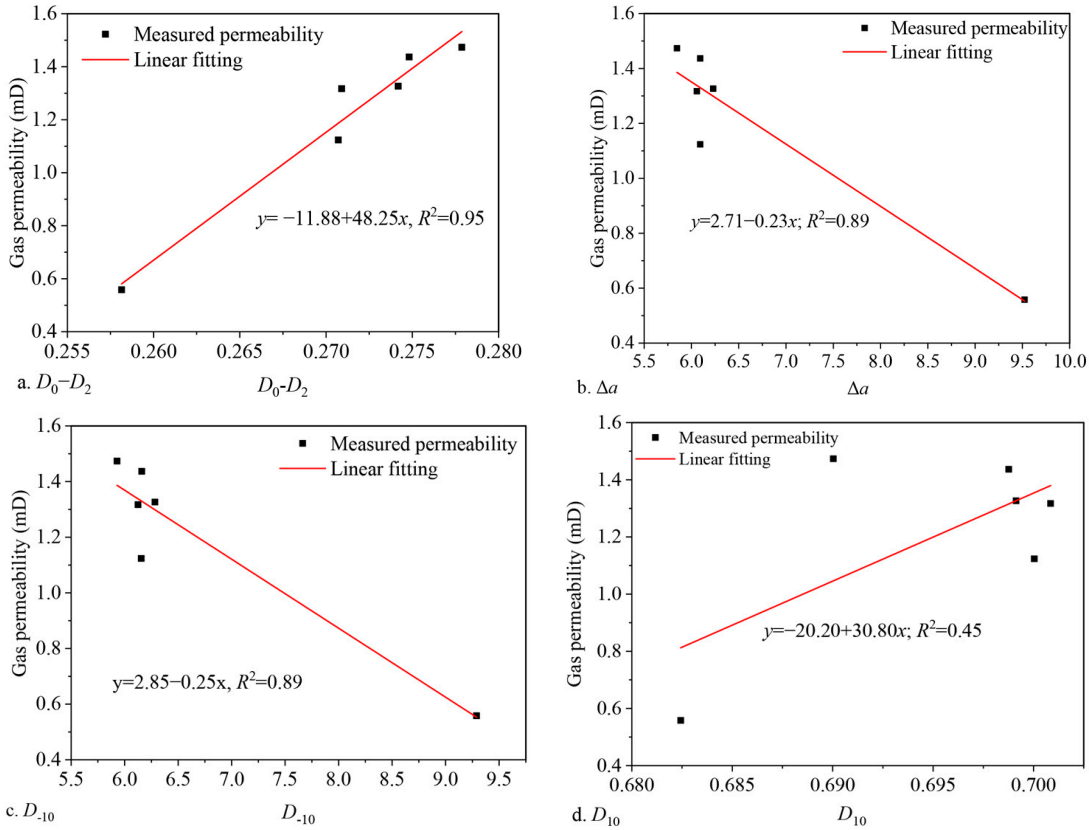

Figure 9. Relationship between multifractal parameters of mobile pore space and permeability. (**a**) D_0-D_2, (**b**) $\Delta\alpha$, (**c**) D_{-10} and (**d**) D_{10}

Firstly, the inverse correlation between D_{-10} (declining from 9.29 to 5.93) and permeability reflects the increasing contribution of large pores and fractures to gas flow (Figure 9c).

D_{-10} typically characterizes the complexity of the distribution of larger pore structures (e.g., flow pores and fractures), with higher values indicating more dispersed. At high water saturation (S_w = 0.88), a high D_{-10} value of 9.29 suggests that water occupies large pore spaces, forming isolated water films or bridges that obstruct flow paths. As centrifugal force increases and water is displaced (S_w decreased to 0.64), the mobile space in large pores is released (from 40.2k to 63.3k units), D_{-10} drops significantly, and pore distribution becomes more ordered, reducing flow resistance in large pores and fractures, thereby increasing permeability. Thus, the negative correlation between D_{-10} and permeability essentially reflects the suppression of large-pore connectivity by structural heterogeneity.

Secondly, the positive correlation between D_{10} (rising from 0.68 to 0.70) and permeability indicates that refining the micropore architecture—particularly within adsorption pores—facilitates gas transport (Figure 9d). D_{10} quantifies small-scale pore structure, with higher values reflecting a narrower size distribution and smoother pore walls. Although these fine pores are not the main conduits for flow, their more uniform geometry reduces capillary trapping of residual water, encourages detachment of water films from pore surfaces, and expands the effective interface between neighboring pathways, thereby improving network connectivity.

The decrease in $\Delta\alpha$ (heterogeneity parameter, from 9.52 to 5.85) and the associated increase in permeability indicate a global structural homogenization that optimizes flow efficiency (Figure 9b). $\Delta\alpha$ represents the width of the multifractal spectrum, with larger values denoting more uneven pore size distributions. At the initial centrifugation stage (3000R), a high $\Delta\alpha$ (9.52) indicates strong heterogeneity, with coexisting micropores and isolated macropores forming tortuous flow paths easily blocked by residual water. As the centrifugal pressure intensifies, $\Delta\alpha$ decreases, indicating a narrowing of pore size distribution, increased proportion of medium-to-large pores, and more coordinated spatial arrangement, forming continuous low-resistance flow networks. This process reduces randomness in flow paths and local bottlenecks, significantly enhancing gas permeability.

Finally, the positive correlation of D_0-D_2 (increasing from 0.258 to 0.278) further validates the central role of pore connectivity in permeability enhancement (Figure 9a). D_0 (box dimension) reflects the space-filling capacity of the pores, while D_2 (information dimension) indicates the degree of distribution clustering. A larger D_0-D_2 value implies better pore system connectivity. The observed increase in D_0-D_2 with increasing centrifugal pressure, alongside the growth in total mobile space (from 56.3k to 103.5k units), indicates that water displacement not only releases pore volume but also reconstructs the pore topology—isolated pores become part of a connected main flow path, forming a hierarchical conductive network. This structural evolution reduces flow tortuosity, leading to a nonlinear enhancement in the permeability response to pore volume changes.

The classical Kozeny–Carman permeability model cannot be evaluated using the current dataset because we did not measure the specific surface area (S_0), hydraulic radius (r_h), or hydraulic tortuosity (τ_{hk}). Any attempt to calculate k_kc without these independently determined inputs would be highly speculative and could lead to misleading conclusions. Future work will include BET/mercury-intrusion measurements and pore-network characterization to enable a robust comparison.

In summary, the gas-phase permeability of coal reservoirs is jointly regulated by multifractal parameters: the reduction in D_{-10} and $\Delta\alpha$ mitigates heterogeneity and releases effective flow space; the increase in D_{10} optimizes micropore interface properties; and the rise in D_0-D_2 strengthens global connectivity of the pore network. This multiscale coupling mechanism suggests that permeability prediction must account for both volumetric expansion and structural homogenization, with the dynamic evolution of fractal

parameters offering a novel theoretical tool for quantitatively characterizing reservoir reformation potential.

4. Conclusions

This study systematically deciphers the dynamic interplay between heterogeneous pore water redistribution and permeability evolution during reservoir depletion through integrated centrifugal-NMR experimentation and multifractal theory. The key scientific contributions are summarized as follows:

(1) Dual-stage pore water redistribution mechanism: Reservoir drainage exhibits scale-dependent fluid migration governed by capillary-adsorption competition. Low-pressure stages (0–0.54 MPa) trigger rapid drainage of fracture and seepage pore water (11.8% total volume loss), while high-pressure stages (0.54–3.83 MPa) concentrate residual water in adsorption pores (95.8% of retained volume). This dual "macropore drainage–micropore retention" behavior underscores the critical role of strong physisorption and nanoconfinement in sustaining structural water heterogeneity under depletion.

(2) Multifractal evolution of pore networks: Multifractal parameters resolve distinct structural controls across drainage phases. At low centrifugal pressure, reduced singularity strength range ($\Delta\alpha$: -36.4%) and capacity-information dimension gap (D_{-10}: -62.1%) signal enhanced macropore connectivity, facilitating initial permeability gains. Conversely, high-pressure regimes amplify adsorption pore heterogeneity (D_0–D_2: +7.8%), reflecting localized water entrapment and interfacial roughness that impede sustained fluid mobility.

(3) Permeability–structure coupling model: A quadratic function links fractal parameters to permeability ($R^2 \geq 0.99$), demonstrating synergistic control by pore volume expansion and structural homogenization. Permeability escalates 3.6-fold as water saturation declines from 1.0 to 0.64, with 63.6% of this enhancement attributable to macropore connectivity gains during early drainage. The nonlinear permeability–water saturation relationship highlights the dominance of flow-path optimization over mere volumetric desaturation.

(4) This work reaffirms the importance of characterizing dynamic permeability evolution within the broader context of reservoir development phases. Each experimental pressure stage corresponds to a specific zone—ranging from early-stage planning to deep mining-affected conditions—each governed by unique capillary pressure, stress regimes, and pore structure evolution. Our findings show that early transition zones facilitate free-water drainage from macropores, while later zones are dominated by the retention of adsorption-bound water in micropores. These insights emphasize the need for adaptive drainage strategies tailored to zone-specific pore characteristics. Moreover, this study establishes a predictive multifractal–permeability coupling framework, deepening our understanding of connectivity thresholds in heterogeneous pore systems. The results offer both theoretical guidance for evaluating dynamic permeability variations and practical strategies for optimizing coalbed methane production in multistage reservoir settings.

(5) Limitations of the study: This work is based on laboratory-scale centrifugal-NMR experiments conducted on a single coal seam sample under controlled conditions. The imposed pressure gradients and small core dimensions may not fully replicate field-scale heterogeneity, reservoir temperature, or geochemical influences. Additionally, coal rank and mineral composition vary across basins, potentially affecting multifractal parameters. Other influencing factors, such as initial saturation conditions,

boundary constraints, and centrifuge acceleration profiles, should be systematically investigated in future studies.

Author Contributions: Conceptualization, F.Q. and H.L.; methodology, W.L.; validation, W.S. and Z.Q.; writing—original draft, F.Q. and Y.S.; writing—review and editing, H.L. and W.S. All authors have read and agreed to the published version of the manuscript.

Funding: This research was funded by the Scientific Research Foundation for High-level Talents of Anhui University of Science and Technology (No. 2023yjrc70), Scientific Research and Development Platform of Technology of Disaster Prevention in Deep Coal Mines, Anhui University of Science and Technology (No. DPDCM2403), and National Natural Science Foundation of China (No. 42402175).

Data Availability Statement: All data, models, and code generated or used during the study appear in the submitted article.

Conflicts of Interest: Wei Lu is employed by State Key Laboratory of Safe Mining of Deep Coal and Environmental Protection, Ltd. The remaining authors declare that the research was conducted in the absence of any commercial or financial relationships that could be construed as a potential conflict of interest.

References

1. Yu, L.; Li, X.; Chong, Z.; Xie, H. Spatial Distribution and Diffusion Characterisation of Water in Coal Samples: An Experimental Study. *Processes* **2024**, *12*, 671. [CrossRef]
2. Zhang, J.; Wei, C.; Chu, X.; Vandeginste, V.; Ju, W. Multifractal Analysis in Characterizing Adsorption Pore Heterogeneity of Middle- and High-Rank Coal Reservoirs. *ACS Omega* **2020**, *5*, 19385–19401. [CrossRef]
3. Tao, S.; Chen, S.; Pan, Z. Current status, challenges, and policy suggestions for coalbed methane industry development in China: A review. *Energy Sci. Eng.* **2019**, *7*, 1059–1074. [CrossRef]
4. Duan, C.; Fu, X.; Deng, Z.; Kang, J.; Zhang, B.; Lu, J.; Hong, X.; Dai, R.; Li, X. Pore Structure Multifractal Characteristics of Coal Reservoirs in the Central and Eastern Qinshui Basin and Influencing Factors. *Processes* **2023**, *11*, 286. [CrossRef]
5. Qin, L.; Lv, S.; Li, S.; Wang, H.; Liu, P.; Mu, M.; Li, J. Freeze–Thaw Response of Permeability and Absorption Channel Structure and Moisture Distribution in Different Coal Ranks. *Nat. Resour. Res.* **2025**, *34*, 1103–1122. [CrossRef]
6. Cheng, G.; Jiang, B.; Li, M.; Li, F.; Xu, S. Quantitative characterization of fracture structure in coal based on image processing and multifractal theory. *Int. J. Coal Geol.* **2020**, *228*, 103566. [CrossRef]
7. Wang, J.; Liu, L.; Cui, Z.; Wang, H.; Li, T.; Duan, L.; Cheng, Y.; Su, P.; Li, M.; Wei, X. Multi-fractal characteristics of pore structure for coal during the refined upgrading degassing temperatures. *J. Pet. Explor. Prod. Technol.* **2021**, *11*, 2931–2942. [CrossRef]
8. Yao, P.; Zhang, J.; Lv, D.; Vandeginste, V.; Chang, X.; Zhang, X.; Wang, D.; Han, S.; Liu, Y. Effect of water occurrence in coal reservoirs on the production capacity of coalbed methane by using NMR simulation technology and production capacity simulation. *Geoenergy Sci. Eng.* **2024**, *243*, 213353. [CrossRef]
9. Zhang, J.; Chu, X.; Wei, C.; Zhang, P.; Zou, M.; Wang, B.; Quan, F.; Ju, W. Review on the Application of Low-Field Nuclear Magnetic Resonance Technology in Coalbed Methane Production Simulation. *ACS Omega* **2022**, *7*, 26298–26307. [CrossRef]
10. Zou, M.; Wei, C.; Zhang, M.; Lv, X. Quantification of gas and water transfer between coal matrix and cleat network during drainage process. *J. Energy Resour. Technol.* **2018**, *140*, 32905. [CrossRef]
11. Ma, Z.; Tao, S.; Gao, L.; Cui, Y.; Jing, Q.; Chen, S.; He, W.; Guo, J.; Hai, L. Detailed characterization of microscopic pore structure in low-rank coal: A case study of zhalainuoer coalfield. *Nat. Resour. Res.* **2024**, *33*, 2261–2277. [CrossRef]
12. Cai, J.; Qin, X.; Xia, X.; Jiao, X.; Chen, H.; Wang, H.; Xia, Y. Numerical modeling of multiphase flow in porous media considering micro-and nanoscale effects: A comprehensive review. *Gas. Sci. Eng.* **2024**, *131*, 205441. [CrossRef]
13. Jahanbakhsh, A.; Wlodarczyk, K.L.; Hand, D.P.; Maier, R.R.J.; Maroto-Valer, M.M. Review of microfluidic devices and imaging techniques for fluid flow study in porous geomaterials. *Sensors* **2020**, *20*, 4030. [CrossRef]
14. Pan, J.; Du, X.; Wang, X.; Hou, Q.; Wang, Z.; Yi, J.; Li, M. Pore and permeability changes in coal induced by true triaxial supercritical carbon dioxide fracturing based on low-field nuclear magnetic resonance. *Energy* **2024**, *286*, 129492. [CrossRef]
15. Wang, X.; Pan, J.; Jin, Y.; Du, X.; Wang, Z.; Cheng, N.; Hou, Q. Morphology and propagation of supercritical carbon dioxide-induced fractures in coal based on a non-destructive surface extraction method. *Fuel* **2025**, *384*, 133948. [CrossRef]

16. Bohaienko, V.; Diele, F.; Difonzo, F.V.; Marangi, C.; Martiradonna, A.; Provenzale, A. Vertical modeling of carbon sequestration in coastal wetlands using fractional-order derivatives and moisture dynamics. *Math. Comput. Simul.* **2025**, *233*, 369–388. [CrossRef]
17. Wang, Z.; Pan, J.; Hou, Q.; Niu, Q.; Tian, J.; Wang, H.; Fu, X. Changes in the anisotropic permeability of low-rank coal under varying effective stress in Fukang mining area, China. *Fuel* **2018**, *234*, 1481–1497. [CrossRef]
18. Li, Q.; Xu, J.; Shu, L.; Yan, F.; Pang, B.; Peng, S. Exploration of the induced fluid-disturbance effect in CBM co-production in a superimposed pressure system. *Energy* **2023**, *265*, 126347. [CrossRef]
19. Pandey, R.; Harpalani, S. An imaging and fractal approach towards understanding reservoir scale changes in coal due to bioconversion. *Fuel* **2018**, *230*, 282–297. [CrossRef]
20. Yu, X.; Xu, H.; Zhai, C.; Regenauer-Lieb, K.; Sang, S.; Sun, Y.; Jing, Y. Characterization of water migration behavior during spontaneous imbibition in coal: From the perspective of fractal theory and NMR. *Fuel* **2024**, *355*, 129499. [CrossRef]
21. Hou, X.; Zhu, Y.; Chen, S.; Wang, Y.; Liu, Y. Investigation on pore structure and multifractal of tight sandstone reservoirs in coal bearing strata using LF-NMR measurements. *J. Pet. Sci. Eng.* **2020**, *187*, 106757. [CrossRef]
22. Zhang, N.; Guo, S.; Wang, S.; Tong, Y.; Li, Z.; Wu, J. Fractal and Multifractal Characteristics on Pore Structure of Coal-Based Sedimentary Rocks Using Nuclear Magnetic Resonance. *SPE J.* **2024**, *29*, 2624–2637. [CrossRef]
23. Zhang, N.; Wang, X.; Wang, S.; Wang, R.; Wu, J.; Li, Z.; Song, Y. Multifractal characteristics on pore structure of Longmaxi shale using nuclear magnetic resonance (NMR). *Geoenergy Sci. Eng.* **2024**, *241*, 213176. [CrossRef]
24. Tao, S.; Chen, S.; Tang, D.; Zhao, X.; Xu, H.; Li, S. Material composition, pore structure and adsorption capacity of low-rank coals around the first coalification jump: A case of eastern Junggar Basin, China. *Fuel* **2018**, *211*, 804–815. [CrossRef]
25. Zhang, Z.; Liu, G.; Liu, H.; Wang, X.; Lin, J.; Barakos, G.; Chang, P. Fractal characterization on methane adsorption in coal molecular structure. *Phys. Fluids* **2024**, *36*, 126611. [CrossRef]
26. Zheng, S.; Sang, S.; Yao, Y.; Liu, D.; Liu, S.; Wang, M.; Feng, G. A multifractal-based method for determination NMR dual T2 cutoffs in coals. *J. Pet. Sci. Eng.* **2022**, *214*, 110488. [CrossRef]
27. Zou, M.; Wei, C.; Huang, Z.; Zhang, M.; Lv, X. Experimental study on identification diffusion pores, permeation pores and cleats of coal samples. *J. Energy Resour. Technol.* **2016**, *138*, 21201. [CrossRef]
28. *SY/T 5346-2005*; Petroleum and Natural Gas Industry Standard. Rock Capillary Pressure Measurement. National Development and Reform Commission of China: Beijing, China, 2005. (In Chinese)
29. Wei, B.; Quan, F.; Song, Y.; Feng, S. Analysis of a middle-rank coal reservoir on a triple porosity/dual permeability model. *Nat. Resour. Res.* **2023**, *32*, 2197–2222. [CrossRef]
30. *SY/T 5336-2006*; Petroleum and Natural Gas Industry Standard. Core Analysis Method. National Development and Reform Commission of China: Beijing, China, 2006. (In Chinese)
31. Mandelbrot, B.B. *The Fractal Geometry of Nature*; W.H. Freeman: New York, NY, USA, 1982; Volume 1.
32. Friesen, W.I.; Mikula, R.J. Fractal dimensions of coal particles. *J. Colloid. Interf. Sci.* **1987**, *120*, 263–271. [CrossRef]
33. Liu, J.; Jiang, B.; Song, Y.; Li, F. Structure and fractal characteristic of micro-and meso-pores in low, middle-rank tectonic deformed coals by CO_2 and N_2 adsorption. *Micropor Mesopor Mat.* **2017**, *253*, 191–202.
34. Martínez, F.S.J.; Martín, M.; Caniego, F.; Tuller, M.; Guber, A.; Pachepsky, Y.; García-Gutiérrez, C. Multifractal analysis of discretized X-ray CT images for the characterization of soil macropore structures. *Geoderma* **2010**, *156*, 32–42. [CrossRef]
35. Zhang, J.; Wei, C.; Ju, W.; Yan, G.; Lu, G.; Hou, X.; Kai, Z. Stress sensitivity characterization and heterogeneous variation of the pore-fracture system in middle-high rank coals reservoir based on NMR experiments. *Fuel* **2019**, *238*, 331–344. [CrossRef]
36. Zhou, S.; Liu, D.; Cai, Y.; Yao, Y. Fractal characterization of pore–fracture in low-rank coals using a low-field NMR relaxation method. *Fuel* **2016**, *181*, 218–226. [CrossRef]
37. Yao, Y.; Liu, D. Comparison of low-field NMR and mercury intrusion porosimetry in characterizing pore size distributions of coals. *Fuel* **2012**, *95*, 152–158. [CrossRef]
38. Yao, Y.; Liu, D.; Che, Y.; Tang, D.; Tang, S.; Huang, W. Non-destructive characterization of coal samples from China using microfocus X-ray computed tomography. *Int. J. Coal Geol.* **2009**, *80*, 113–123. [CrossRef]
39. Zou, M.; Liu, Y.; Huang, Z.; Zhang, M.; Zhang, P. Geological control of irreducible water within the coal matrix and its quantified evaluation model. *ACS Omega* **2020**, *5*, 9540–9549. [CrossRef]
40. Shen, J.; Qin, Y.; Wang, G.X.; Fu, X.; Wei, C.; Lei, B. Relative permeabilities of gas and water for different rank coals. *Int. J. Coal Geol.* **2011**, *86*, 266–275. [CrossRef]
41. Han, L.; Shen, J.; Qu, J.; Ji, C.; Cheng, H. The analysis of the micro-occurrence state of irreducible water in anthracite fracture network based on digital core. *Aapg Bull.* **2023**, *107*, 1781–1797. [CrossRef]
42. Zhang, J.; Quan, F.; Zhang, H.; Shao, Y.; Han, Y.; Yang, Y.; Chang, X.; Zhang, X. Multi-method characterization of sandstone pore size distribution heterogeneity and its influence on porosity and permeability variation. *Front. Earth Sci.* **2024**, *18*, 814–830. [CrossRef]
43. Tian, T.; Zhang, D.; Shi, Y.; Quan, F.; Qin, Z. Pore-Fracture System Distribution Heterogeneity by Using the T2 Spectral Curve under a Centrifugal State. *Processes* **2024**, *12*, 1812. [CrossRef]

44. Li, H.; He, J.; Lu, J.; Lin, B.; Lu, Y.; Shi, S.; Ye, Q. A review of laboratory study on enhancing coal seam permeability via chemical stimulation. *Fuel* **2022**, *330*, 125561. [CrossRef]
45. Connell, L.D. A new interpretation of the response of coal permeability to changes in pore pressure, stress and matrix shrinkage. *Int. J. Coal Geol.* **2016**, *162*, 169–182. [CrossRef]